PHYSICAL REVIEW B **69**, 174509 (2004)

Angle-dependent magnetoresistance of the layered organic superconductor κ-$(\mathrm{ET})_2\mathrm{Cu}(\mathrm{NCS})_2$: Simulation and experiment

P. A. Goddard,[1,*] S. J. Blundell,[2] J. Singleton,[1] R. D. McDonald,[1] A. Ardavan,[2] A. Narduzzo,[2] J. A. Schlueter,[3]
A. M. Kini,[3] and T. Sasaki[4]
[1]*National High Magnetic Field Laboratory, Los Alamos National Laboratory, TA-35, MS-E536, Los Alamos, New Mexico 87544, USA*
[2]*Department of Physics, University of Oxford, Clarendon Laboratory, Parks Road, Oxford OX1 3PU, United Kingdom*
[3]*Materials Science Division, Argonne National Laboratory, Argonne, Illinois 60439, USA*
[4]*Institute for Materials Research, Tohoku University, Sendai 980-77, Japan*

(Received 3 December 2003; revised manuscript received 17 March 2004; published 28 May 2004)

The angle dependences of the magnetoresistance of two different isotopic substitutions (deuterated and undeuterated) of the layered organic superconductor κ-$(\mathrm{ET})_2\mathrm{Cu}(\mathrm{NCS})_2$ are presented (where ET is the organic molecule bis(ethylenedithio)-tetrathiafulvalene). The angle-dependent magnetoresistance oscillations (AMRO) arising from the quasi-one-dimensional and quasi-two-dimensional Fermi surfaces in this material are easily confused. By using the Boltzmann transport equation extensive simulations of the AMRO are made that reveal the subtle differences between the different species of oscillation. No significant differences are observed in the electronic parameters derived from quantum oscillations and AMRO for the two isotopic substitutions. The interlayer transfer integrals are determined for both isotopic substitutions and a slight difference is observed which may account for the negative isotope effect previously reported. The success of the semiclassical simulations suggests that non-Fermi liquid effects are not required to explain the interlayer transport in this system.

DOI: 10.1103/PhysRevB.69.174509 PACS number(s): 74.70.Kn, 71.20.Rv

I. INTRODUCTION

κ-$(\mathrm{ET})_2\mathrm{Cu}(\mathrm{NCS})_2$ is probably the most popular and best characterized material out of all the organic charge-transfer salts based on the ET molecule. Its attraction to experimentalists lies in its exceedingly simple Fermi surface, which consists of two elliptical quasi-two-dimensional (Q2D) pockets and a pair of warped quasi-one-dimensional (Q1D) sheets[1,2] (see Fig. 1). The prospect of understanding the complex transport properties of the organic salts seems more within reach for this material than for others that show similar behavior but have more complicated Fermi surfaces.

Several theoretical models of the unconventional superconductivity observed in κ-$(\mathrm{ET})_2\mathrm{Cu}(\mathrm{NCS})_2$ and related materials suggest that the superconducting pairing mechanism may be mediated by antiferromagnetic spin fluctuations.[3–5] These models are found to be sensitive to the degree to which the Fermi surface of the material can nest; the higher the nestability, the more likely this pairing is to be successful. Two-dimensional Fermi surfaces are clearly better able to nest than three-dimensional ones, and so tests of the dimensionality of κ-$(\mathrm{ET})_2\mathrm{Cu}(\mathrm{NCS})_2$ also test these theoretical models.

In this paper the low-temperature angle dependence of the magnetoresistance in deuterated and undeuterated samples of κ-$(\mathrm{ET})_2\mathrm{Cu}(\mathrm{NCS})_2$ is studied in detail in magnetic fields significantly higher than in-plane upper critical field. The purpose of this is to completely determine the parameters that define the transport in this material, to locate any differences between these parameters for the two isotopic substitutions that might shed light on the disparity between their superconducting critical temperatures,[6] and to address the question of whether it is possible to describe all aspects of the normal-state transport within the bounds of Fermi liquid theory.

As with all the organic conductors in this class, the ET molecules form the highly conducting layers, separated by layers of the anion, with the long axis of the ET molecule at a small angle to the interlayer direction. In the κ-phase salts the ET molecules associate into pairs, or dimers, each of which collectively donates one electron to the anions, leaving behind a mobile hole.[7] There are two dimers, and thus two holes per unit cell, and so, because the dispersion is nearly isotropic in the bc plane, this leads to a roughly circular Fermi surface which has the same area as the first Brillouin zone.[1] The Brillouin zone itself reflects the rectangular cross section of the unit cell and the Fermi surface cuts the Brillouin zone boundaries on its long side. At these points a gap opens up which splits the Fermi surface into the Q1D and Q2D sections.[1,2] The result is shown in the top part of Fig. 1.

The shape of the Fermi surface in the k_xk_y plane has been confirmed by the observation of magnetic quantum oscillations.[1,8] The frequency of the quasiparticle orbits about the circumference of the Q2D pockets (α orbits) is found to be 600 T which corresponds to about 15% of A_{BZ}, the area of the cross section of the first Brillouin zone in the k_xk_y plane.[8] Above 20 T magnetic breakdown is observed as it becomes possible for some of the quasiparticles to bridge the energy gap between the two Fermi surface sections and make the large β orbit, whose frequency is found to be 3920 T.[8] This corresponds to an area equal to A_{BZ} to within a few percent, as would be expected from the considerations discussed above.

κ-$(\mathrm{ET})_2\mathrm{Cu}(\mathrm{NCS})_2$ has a monoclinic structure and the transfer integral between the layers lies parallel to the a lattice parameter which is inclined at an angle of 110.3° to the

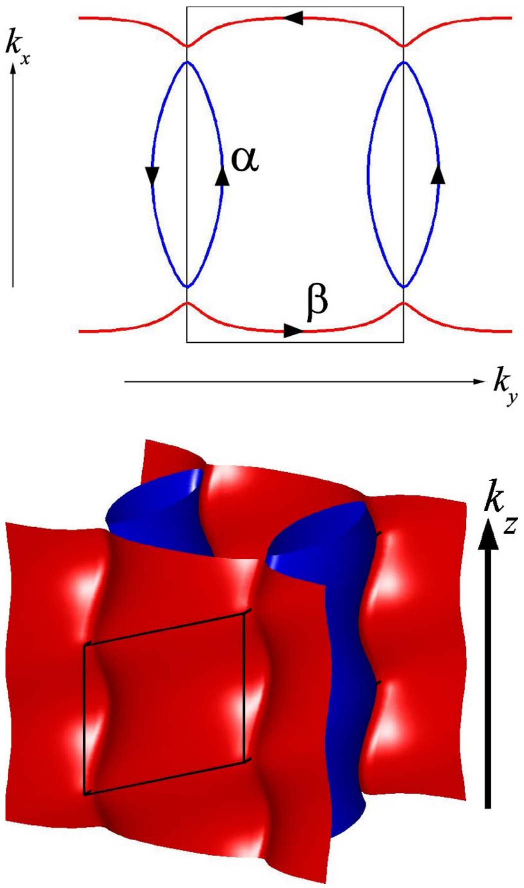

FIG. 1. Top: Cross section of the Fermi surface of κ-(ET)$_2$Cu(NCS)$_2$ in the k_xk_y plane. The shape is defined by three transfer integrals in the highly conducting layers [see Eq. (1)]. Bottom: The same Fermi surface in three dimensions. The interlayer warping is defined by the transfer integral t_a [see Eq. (6)], and is exaggerated for clarity.

highly conducting bc planes.[7] This transfer integral t_a is much smaller than those within the planes and results in a slight warping of the Fermi surface perpendicular to the direction of t_a in k space. This is shown in the lower portion of Fig. 1. The validity of this picture of the Fermi surface as a three-dimensional object is discussed in Ref. 9.

II. OVERVIEW OF THE FEATURES OBSERVED IN MAGNETOTRANSPORT

Figure 2 shows two typical θ dependences (where θ is the angle between the magnetic field and the normal to the conducting layers) of the interlayer magnetoresistance of κ-(ET)$_2$Cu(NCS)$_2$ in fixed magnetic fields of 27 T and 42 T and at an azimuthal angle of 149°. In such high fields a whole host of features are observed in an interlayer transport measurement of κ-(ET)$_2$Cu(NCS)$_2$, e.g., Shubnikov-de Haas (SdH) oscillations, magnetic breakdown, and Q1D and Q2D angle-dependent magnetoresistance oscillations (AMRO). This means that for a typical θ rotation, the magnetoresistance is rich in features as Fig. 2 illustrates.

The upper plot shows the data taken at 42 T and the lower at 27 T. In the upper plot the field perpendicular to the layers around $\theta = 0°$ is sufficient for the effects of magnetic breakdown to be observed and the fast SdH oscillations due to the β orbit are clearly seen. The slower oscillations due to the α orbit are seen in both plots and persist to higher angles. The amplitudes of these oscillations are modulated and they disappear at certain θ angles; these nodes are known as *spin zeros* and are caused by Zeeman splitting of the Landau levels.[10] An analysis of this effect is dealt with in Sec. V B.

The positions of the features at θ angles greater than about $\pm 70°$ are seen to be independent of the magnitude of the magnetic field, which reveals them to be AMRO of one variety or another. Four different types of AMRO are possible in the interlayer resistivity (ρ_{zz}) of κ-(ET)$_2$Cu(NCS)$_2$. These are the Danner-Kang-Chaikin oscillations,[11] the third angle effect[12] and the Lebed magic angle effect[13] which all arise from orbits on the Q1D Fermi surface section, and the Yamaji oscillations arising from orbits on the Q2D Fermi surface section.[14,15] In the semiclassical picture all the AMRO are caused by the degree to which the velocity components of the quasiparticle are averaged over the series of orbits that appear at a certain inclination angle. In particular, the orbits that are possible in the region of the Yamaji angles are very successful in averaging the interlayer velocity towards zero, thus peaks are seen in the interlayer resistance.[14,15] In contrast, the orbits that occur at the Lebed magic angles are not as successful at averaging the interlayer velocity towards zero as those possible at the other angles and so dips in ρ_{zz} are observed.[13] There are other theories that can explain the effects observed at the Lebed magic angles. Lebed's own argument describes electron-electron correlations whose magnitudes change when the field is directed along the magic angles.[16] Another theory has regions of k space where the scattering rate takes a large value (Fermi-surface hotspots) accounting for the AMRO.[17] However, such theories are complicated and need only be invoked when the semiclassical approach fails to account for the experimental observations. It will be shown by the simulations described in Sec. V C that the semiclassical explanation is sufficient in the case of κ-(ET)$_2$Cu(NCS)$_2$.

In the upper plot of Fig. 2, a small peak is observed when the field lies very close to the in-plane direction, $\theta \approx 90°$. This is the in-plane peak feature mentioned in Ref. 9. It will be discussed further in Sec. V D. Around $\theta = 90°$ in the lower plot, the in-plane peak is obscured by the large dip that indicates the onset of a superconducting transition. This occurs because there is a considerable anisotropy in the upper critical field of this material, and a field of 27 T is not sufficient to suppress the superconducting state when applied in a nearly in-plane direction.[18]

It should also be noted from Fig. 2 that the amplitude of all the features in the magnetoresistance increases with increasing field, and that the plots are not symmetrical about $\theta = 0°$, reflecting the monoclinic symmetry of the crystal structure.

III. PARAMETRIZING THE FERMI SURFACE

It has been shown that the measured intralayer Fermi surface of κ-(ET)$_2$Cu(NCS)$_2$ can be reproduced using a disper-

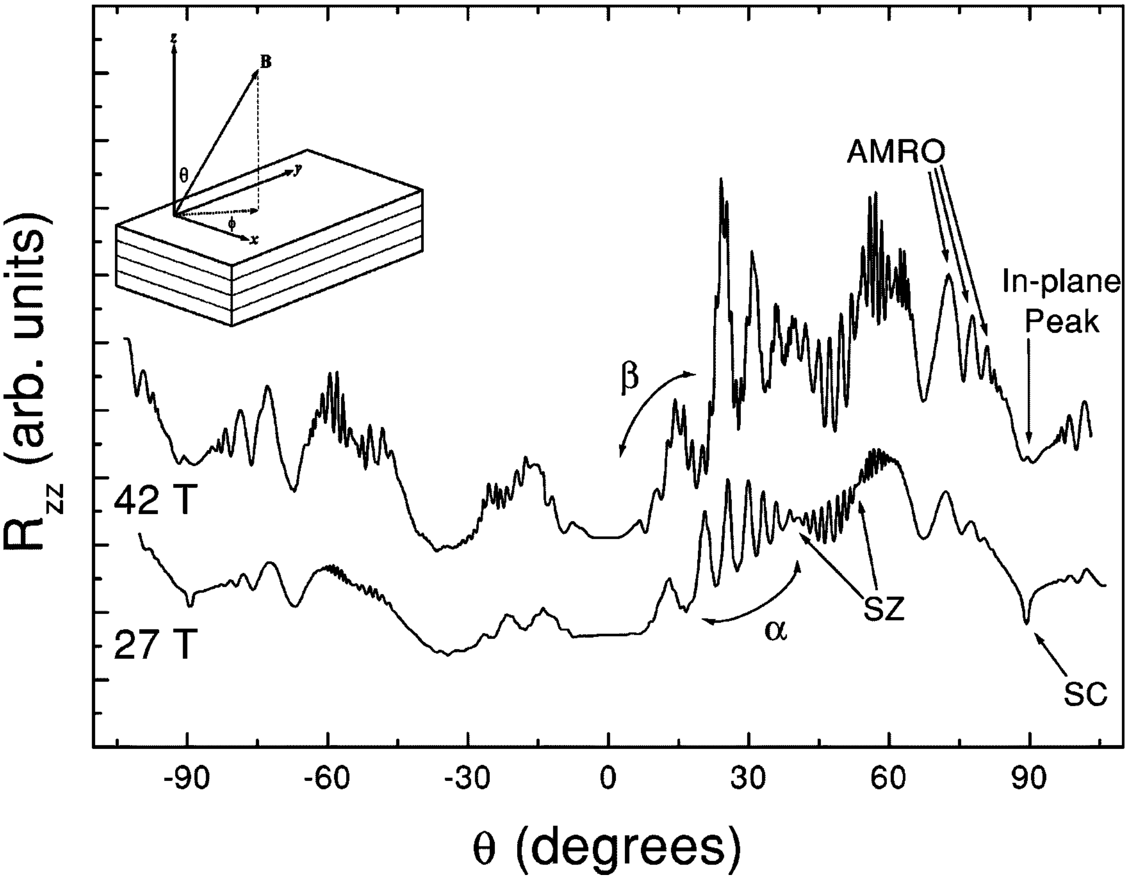

FIG. 2. Typical θ dependence of the magnetoresistance of κ-(ET)$_2$Cu(NCS)$_2$. The data shown is for a hydrogenated sample at 490 mK, $\phi = 149°$ (where ϕ is the azimuthal angle), 27 T (lower), and 42 T (upper). The data have been offset for clarity. Some representative features are indicated; SdH oscillations due to the Q2D pockets (α) and the breakdown orbit (β); spin zeros in the SdH amplitudes (SZ); the onset of the superconducting transition (SC); angle-dependent magnetoresistance oscillations (AMRO), whose positions are field independent; and the resistive peak in the presence of an exactly in-plane magnetic field (In-plane Peak). The inset diagram is included to illustrate the measurement geometry.

sion relation derived from a tight-binding model using the ET dimer as its base unit.[3,8,9] In this way the intradimer transfer integral t_d can be ignored and shape of the Fermi surface depends upon interdimer transfer integrals t_b, t_{c1}, t_{c2} and the Fermi energy E_F. The dispersion found in this manner is known as the *effective dimer model* and is given by

$$E(\mathbf{k}) = 2t_b \cos(k_x b) \pm \cos\left(\frac{k_x b}{2}\right)\sqrt{t_{c1}^2 + t_{c2}^2 + 2t_{c1}t_{c2}\cos(k_y c)}, \qquad (1)$$

where the $+$ and $-$ signs result in the Q1D and the Q2D sections of the Fermi surface, respectively.[3,8]

The effective dimer model is used in the semiclassical calculations of Secs. V C and V D. These do not take account of quantum effects such as Shubnikov–de Haas (SdH) oscillations or magnetic breakdown, and are assumed to be in the "low-field" region where breakdown does not occur. It will be seen that this is a reasonable assumption in both cases. This means that the effect of the energy gap, i.e., the difference between t_{c1} and t_{c2}, can at first be neglected and the shape of the in-plane Fermi surface depends only upon the ratios E_F/t_c and t_b/t_c, where t_c is an average of t_{c1} and t_{c2}.[3,9]

It is possible to obtain values for these ratios by adjusting them to reproduce the areas of the α and β Fermi-surface orbits. Once this is done, t_b, t_c, and E_F can be uniquely specified by fitting to the effective mass of the β orbit as found from SdH oscillations, using the expression $\delta A_\beta/\delta E = 2\pi m_\beta^*/\hbar^2$.[19] Note that it also possible to fit to the mass of the α orbit to obtain slightly different results. However, as the masses are derived from quantum oscillations, they are orbitally averaged, and so the α mass will be dominated by the extremely pointed regions of the Q2D pockets. The breakdown orbit does not have these pointed regions and thus it is the β mass that is used in the fitting procedure.

The energy gap can now be reintroduced in order to specify t_{c1} and t_{c2}. In the region of the gap, $\cos(k_c c) = -1$ and $\cos(k_b b/2) \approx 0.5$, so that $E_g \approx 2(t_{c1} - t_{c2})$. From the magnetic breakdown, E_g is estimated to be 7.8 meV.[9,20] Any inaccuracies in this value will not lead to errors in the size of the Fermi surface produced by Eq. (1), but could lead to small discrepancies in the exact dimensions of the α pocket.

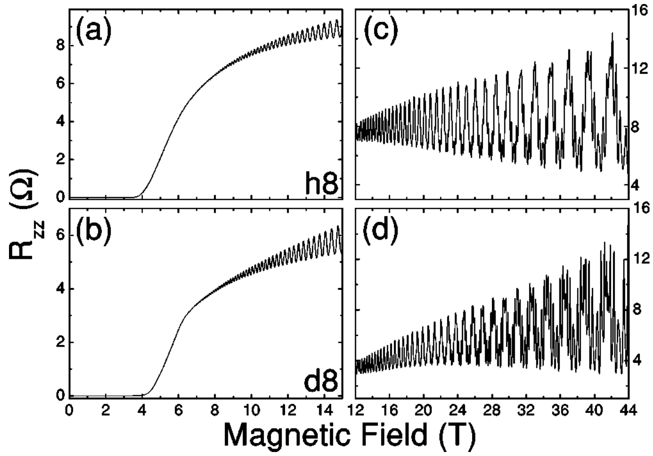

FIG. 3. Comparison of the SdH oscillations observed in the interplane magnetoresistance of $h8$ and $d8$ κ-$(ET)_2Cu(NCS)_2$. (a) and (b) show the low-field region of $h8$ and $d8$, respectively, at a temperature of 620 mK. The superconducting transition and the SdH oscillations arising from the α orbit are clearly seen. (c) and (d) show the high-field region of $h8$ and $d8$, respectively, at a temperature of 480 mK. The onset of magnetic breakdown is apparent in both samples, although the breakdown oscillation seems to be more dominant in the $d8$ than the $h8$.

The Fermi-surface parameters obtained in this manner are as follows: $t_b = 14.87$ meV; $t_{c1} = 26.65$ meV; $t_{c2} = 22.75$ meV; and $E_F = -19.12$ meV. Note that these values of t are effective transfer integrals, and incorporate the effects of electron-phonon and electron-electron interactions as they are derived from magnetic quantum oscillation data (see Ref. 21 for a discussion). Note also that E_F is taken relative to the zero energy of the effective dimer model and not the bottom of the band. It should therefore *not* be quoted as the Fermi energy of κ-$(ET)_2Cu(NCS)_2$.

IV. EXPERIMENTAL DETAILS

Four single-crystal samples of κ-$(ET)_2Cu(NCS)_2$ were used in this study, made using an electrocrystallization method[6] (and references therein). All of the samples are black platelets of the order of $0.7 \times 0.5 \times 0.1$ mm^3, with the plane of the plate corresponding to the highly conducting layers. In one of the samples the eight terminal hydrogens of the ET molecules were substituted by deuterium. In what follows the deuterated crystal will be referred to as $d8$ and the hydrogenated crystals as $h8$.

The magnetoresistance measurements were made using standard four-wire ac techniques ($f = 50$–180 Hz) with the current applied in the interplane direction ($I = 1$–20 μA).

All the samples were mounted on a two-axis rotator in a ^{3}He cryostat. In this rotator it is possible to continuously change the θ angle, the angle between the magnetic field and the highly conducting bc planes, and discretely change the plane of rotation, described by the azimuthal angle ϕ. An angular calibration technique similar to that described in Ref. 22 was used when misalignments of the sample that occur during cooling were found to be significant. Temperatures down to 0.5 K are readily accessible.

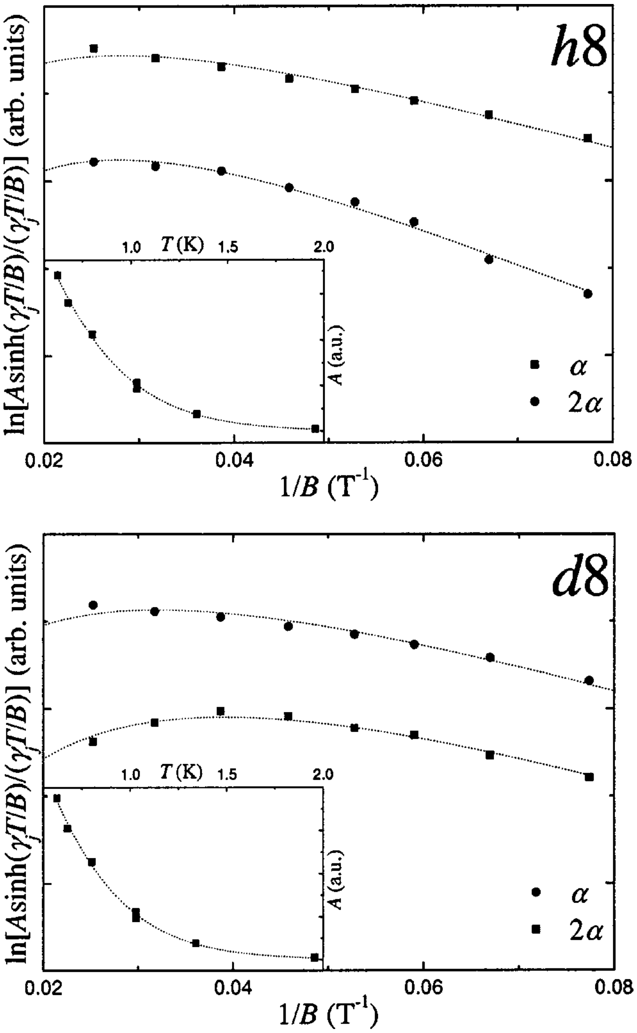

FIG. 4. The result of fitting the Fourier amplitude A of the $h8$ (top) and $d8$ (bottom) α frequency (squares) and its second harmonic (circles) to the two-dimensional Lifshitz-Kosevich formula at constant temperature, over a field range of 12–44 T, using the technique outlined in the text and Ref. 20. This kind of analysis yields values for the scattering time and the magnetic breakdown field. The insets show the result of fitting the temperature dependence of the $h8$ (top) and $d8$ (bottom) α frequency amplitude over a constant (low-)field interval. The $h8$ and $d8$ data at each temperature were taken simultaneously and the fact that the insets are similar is an indication that the effective masses of the two isotopic substitutions are also similar.

V. RESULTS AND DISCUSSION

A. The Shubnikov–de Haas oscillations

Figure 3 shows the SdH oscillations observed in the high- and low-field regions for both $h8$ and $d8$ samples at pumped ^{3}He temperatures. Using the results of a fast Fourier transform analysis of several SdH measurements, the fundamental frequencies were found to be $F_\alpha(h8) = 599 \pm 3$ T; $F_\beta(h8) = 3860 \pm 6$ T; $F_\alpha(d8) = 598 \pm 3$ T; and $F_\beta(d8) = 3871 \pm 10$ T—all of which are in reasonable agreement with previous results.[8,23]

The α mass of $h8$ κ-$(ET)_2Cu(NCS)_2$ has previously been found to be $m_\alpha^*(h8) = 3.5 \pm 0.1$ m_e (Ref. 8) using a

Lifshitz-Kosevich analysis of the temperature dependence of the SdH amplitudes.[19] Using the same method the equivalent $d8$ mass is $m_\alpha^*(d8)=3.6\pm0.1\ m_e$.

The Lifshitz-Kosevich analysis can also be applied to the field dependence of the SdH amplitudes at a constant temperature to find values for the scattering time (τ) and the breakdown field (B_0). Using the technique outlined in Ref. 20 (but correcting the erroneous minus sign that prefixes the breakdown term in that reference), the measured amplitudes A are fitted with the function,

$$\ln\left[\frac{A\sinh(\gamma_j T/B)}{\gamma_j T/B}\right]=\ln[A_0]-\frac{\gamma_j T_{\mathrm{D},j}}{B}+\ln[p^{n_{1j}}q^{n_{2j}}], \quad (2)$$

where A_0 is a constant, $\gamma_j=(2\pi^2\mu_j^* l_j k_{\mathrm{B}})/(\hbar e)$, $p^2=\exp(-B_{0j}/B)$, and $q^2=1-p^2$.[19] T_{D} is the Dingle temperature and is proportional to the scattering rate, $\mu_j^*=m_j^*/m_e$, m_e is the mass of an electron, l_j is the harmonic index of the orbit, n_{1j} is the number of magnetic breakthrough points on the orbit, and n_{2j} is the number of Bragg reflection points.[19] Note that this is derived from the two-dimensional form of the Lifshitz-Kosevich formula with the magnetic field directed perpendicular to the highly conducting layers. The amplitudes are obtained from the fast Fourier transform spectrum of the oscillating part of the resistance. The field window over which the Fourier transform is performed specifies the value of B in the above equation such that $B^{-1}=(B_1^{-1}+B_2^{-1})/2$, where B_1 and B_2 are, respectively, the start and end points of the field window.[24]

The functional form of the T_{D} and B_0 terms in the Lifshitz-Kosevich formula are similar and so to obtain a satisfactory fit the amplitudes of the first and second harmonics of the α frequency must be fitted simultaneously.[20] In this case $n_1(\alpha)=n_1(2\alpha)=0$, $n_2(\alpha)=2$ and $n_2(2\alpha)=4$. Thus, at high fields these amplitudes are attenuated as quasiparticles are able to tunnel across the gap to the β orbit. The fits are shown in Fig. 4 and the values obtained are $\tau(h8)=2.3\pm0.2$ ps; $\tau(d8)=2.4\pm0.2$ ps; $B_0(h8)=58\pm9$ T; and $B_0(d8)=39\pm10$ T. The values of the scattering time obtained from the high-field fits are in close agreement with those obtained from a fit to the low-field data where the effects of breakdown may be neglected.

Note that all the results for the $d8$ sample are the same as those for the $h8$ within the experimental errors. The large errors on the values of the breakdown field and the discrepancies between these values and those independently obtained from similar data [$B_0(h8)=41\pm7$ T, Ref. 20] and even the same dataset [$B_0(h8)=41\pm5$ T and $B_0(d8)=30\pm5$ T, Ref. 23] serve to highlight the limitations of the Lifshitz-Kosevich formula at high fields,[25] where not only is there competition between two functionally similar terms, but also the amplitudes of the quantum oscillations become very large. Despite coinciding at the extremes of their error margins, the mean values of B_0 obtained here (and those obtained in Ref. 23) suggest that the breakdown field for $d8$ is significantly smaller than that for $h8$, which would explain why the breakdown oscillations shown in Fig. 3 appear more dominant in the deuterated salt.

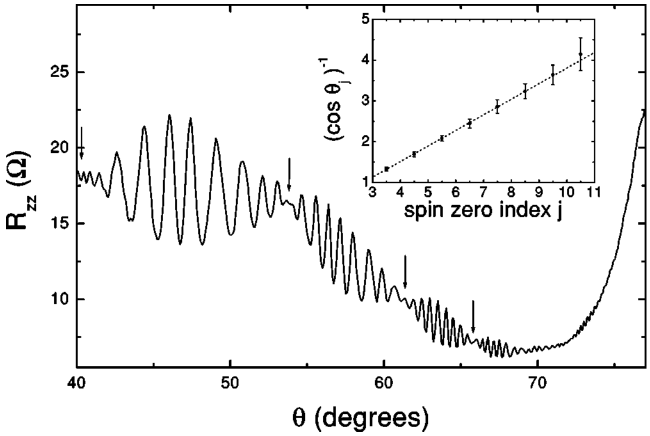

FIG. 5. The spin-zero effect as seen in a typical θ dependence of the magnetoresistance of κ-(ET)$_2$Cu(NCS)$_2$. The data shown is for an $h8$ sample at 590 mK, $\phi=90.8°$, and 27 T. The spin-zero angles θ_j are indicated by arrows. The data points in the inset are a summary of the θ_j observed at a number of different azimuthal angles, magnetic fields, and in two different single-crystal samples. The broken line is a straight line fit to these data.

B. The effect of spin splitting

The energy levels of a quasiparticle in a metallic system subjected to an applied magnetic field are defined by Landau quantization and the Zeeman effect, and are given by

$$E=\left(n+\frac{1}{2}\right)\frac{\hbar eB\cos\theta}{m^*}\pm\frac{1}{2}g^*\mu_{\mathrm{B}}B, \quad (3)$$

where n is the Landau level index and g^* is the effective g factor.[26] Increasing the θ angle reduces the separation between Landau levels by reducing the field perpendicular to the highly conducting planes, $B\cos\theta$. When $B\cos\theta$ is such that the spin-up and spin-down sections of different Landau levels are degenerate, then the separation between successive energy levels is equal to $\hbar\omega_c$. At this angle the SdH oscillations having the fundamental frequency F will dominate, taking their maximum amplitude. However, when $B\cos\theta$ is such that the spin-up and spin-down sections of different Landau levels are equally spaced at $\frac{1}{2}\hbar\omega_c$, then the dominant oscillations will be those with frequency $2F$ and the amplitude of the fundamental oscillations will be at a minimum.[10] These two situations are known as spin maxima and spin zeros, respectively.

It is easy to show that the conditions for spin zeros and spin maxima are given by[10]

$$g^*\mu_{\mathrm{B}}B=j\,\frac{\hbar eB\cos\theta}{m^*}\begin{cases} j=\frac{1}{2},\frac{3}{2},\frac{5}{2}\ldots & \text{spin zero}\\ j=1,2,3\ldots & \text{spin max.}\end{cases} \quad (4)$$

As has already been mentioned, this effect can be observed as a modulation of the α-frequency SdH oscillations when a crystal of κ-(ET)$_2$Cu(NCS)$_2$ is rotated in a fixed field. Figure 5 shows a typical section of such a rotation for an $h8$-sample, and several spin-zero angles θ_j are marked with arrows. The inset shows a plot of $(\cos\theta_j)^{-1}$ versus j index. This dataset is a summary of a large number of spin-

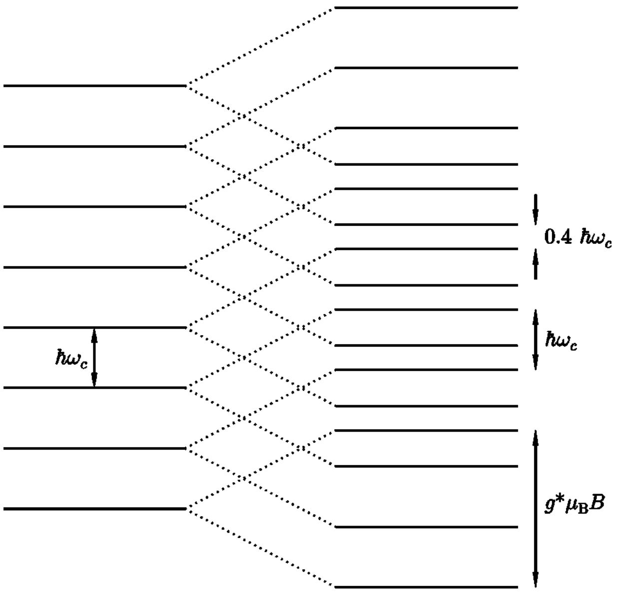

FIG. 6. The energy-level spectrum of κ-(ET)$_2$Cu(NCS)$_2$ at $\theta = 0°$ as deduced from $g^*\mu_\alpha^* \approx 5.2$, measured at ~ 0.5 K in the low-field region. There are two splittings, one of $\hbar\omega_c$, which results in the SdH oscillations of the fundamental frequency, and one of $0.4\ \hbar\omega_c$, which at sufficiently low temperatures and high fields will result in the observation of harmonics of the fundamental frequency.

zero positions measured at many different values of the azimuthal angle, at fields of 27 and 42 T, and in two different single crystals. Using the gradient of the straight-line fit shown, the product of the effective g factor and μ^*, where $\mu^* = m^*/m_e$, is found to be $g^*\mu_\alpha^*(h8) = 5.22 \pm 0.56$.

The dataset for $d8$ is not as extensive as that for $h8$, nevertheless a good fit is still achieved, yielding $g^*\mu_\alpha^*(d8) = 5.24 \pm 0.65$. The values for $h8$ and $d8$ are identical within the errors.

The value for $g^*\mu_\alpha^*(h8)$ obtained here appears to be in good agreement with that of Ref. 27, obtained by fitting three spin-zero points from de Haas–van Alphen data. In that reference the authors assume that $g^* = 2$ and that the mass obtained from the spin-zero effect is renormalized by electron-electron interactions, but not electron-phonon interactions. They then use the difference between this mass and that derived from a Lifshitz-Kosevich analysis of quantum oscillations to specify the electron-phonon coupling constant.[27] However, as the $g^*\mu^*$ values obtained in this manner may not be renormalized in the same way as the effective masses found from the thermodynamic variation of the quantum oscillation amplitudes or the g factors obtained from electron-spin resonance; it is not advisable to separate g^* and μ^* in this fashion.

It is possible, using the experimentally determined value of $g^*\mu^*$, to make a comparison of the spin and Landau level splittings. The ratio of the splittings at $\theta = 0°$ is given by

$$\frac{g^*\mu_B B}{\hbar\omega_c} \equiv \frac{g^*\mu^*}{2}, \tag{5}$$

using $\omega_c = eB/m^*$ and $\mu_B = e\hbar/2m_e$. So for both $h8$ and $d8$ the ratio of the spin to Landau level splitting is around 2.6, which results in the energy-level diagram shown in Fig. 6. It is seen that as well as the energy splitting of $\hbar\omega_c$ between one spin split level and its equivalent from the next highest Landau level, there exists another splitting, of $0.4\ \hbar\omega_c$, arising from the difference between the spin-up of one Landau level and the spin-down of the Landau level three places up.

C. The angle-dependent magnetoresistance oscillations

1. Boltzmann transport simulations

An analysis of the angular effects in κ-(ET)$_2$Cu(NCS)$_2$ is complicated by the coexistence of Q1D and Q2D Fermi surfaces. The method by which the different types of AMRO either dominate or superpose over one another is not at all clear, depending as it does on unknowns such as the relative effective masses and carrier densities of the quasiparticles on the Q1D and Q2D sections. To further complicate an AMRO investigation it should be noted that in general Lebed magic angles and Yamaji oscillations can be analyzed in very similar ways. For example, if the resistive peaks that lie between dips caused by the Q1D Lebed magic angle effect are accidently mistaken for Q2D Yamaji oscillations, it is possible, as will be shown later, to obtain the dimensions of a closed Fermi surface pocket that may appear reasonable, but are incorrect. For this reason, when measuring samples whose Fermi surface is uncharted, the Lebed magic angles and Yamaji oscillations are best used in conjunction with other Fermi-surface effects such as Danner-Kang-Chaikin, or quantum oscillations, which specify exclusively the nature of the Fermi surface from which they arise.

In the sample under review here, the presence of both Q1D and Q2D sections of Fermi surface is not in question as it is demonstrated convincingly by the magnetic breakdown observed in the SdH effect. However, in order to make sense of the AMRO data measured experimentally, some method of separating the oscillations arising from the two sections is required. This is achieved by making detailed, semiclassical simulations of the interplane resistivity resulting from the Q1D and Q2D Fermi surfaces. A suite of programs were therefore developed which used Fortran (for operational speed) to solve the equations of motion for any specified Fermi surface and field orientation and use the results of this to find a numerical solution to the Chambers formula [Eq. (7) below]. This software was applied to model Fermi surfaces and the AMRO results were seen to agree with theoretical predictions.

It is necessary here to simulate the angle-dependent effects observed in κ-(ET)$_2$Cu(NCS)$_2$. To this end an equation that describes the entire Fermi surface of this material throughout the first Brillouin zone is formulated

$$\begin{aligned} E(\mathbf{k}) = {} & 2t_b\cos(k_x b) \pm \cos\left(\frac{k_x b}{2}\right) \\ & \times \sqrt{t_{c1}^2 + t_{c2}^2 + 2t_{c1}t_{c2}\cos(k_y c)} \\ & - 2t_a\cos\left[k_z a\cos\left(\beta - \frac{\pi}{2}\right) - k_y a\sin\left(\beta - \frac{\pi}{2}\right)\right], \end{aligned} \tag{6}$$

in which the conducting layers of the ET molecules lie in the bc- (or xy-)plane, β is the angle between the crystallographic a and c directions, and the z axis lies along the interlayer direction. The first two terms of the equation are simply the effective dimer model that was discussed previously and which is known to accurately describe the intralayer Fermi surface. The last term is a tight-binding representation of the interlayer dispersion. For the purposes of the simulations, the values of t_b, t_{c1}, t_{c2} and the Fermi energy are set to be those quoted earlier, derived from a consideration of experimental results. The transfer integral t_a is set to be 0.04 meV. This is the value resulting from a preliminary investigation of the in-plane peak effect.[9,28]

As a quasiparticle moves across the Fermi surface under the influence of the magnetic field, its component of velocity in a given direction will vary as it negotiates the various Fermi-surface contours and corrugations (its total velocity remaining perpendicular to the Fermi surface at all times). Considering an entire Fermi surface filled with orbiting quasiparticles it is not difficult to see that the combination of these varying velocity components leads to a conductivity that depends strongly on the nature of the orbits and the geometry of the Fermi surface.

This argument is formalized in the isothermal solution to the Boltzmann transport equation known as the Chambers formula,

$$\sigma_{ij}=\frac{e^2}{4\pi^3}\int d\,\mathbf{k}^3\left(-\frac{df_0}{d\varepsilon}\right)v_i(\mathbf{k},0)\int_{-\infty}^{0}v_j(\mathbf{k},t)e^{t/\tau}dt, \quad (7)$$

where σ_{ij} is a component of the conductivity tensor, f_0 is the unperturbed quasiparticle (Fermi-Dirac) distribution function, v_i and v_j are velocity components, and $1/\tau$ is the $\mathbf{k}$-independent scattering rate.[29] This equation represents a velocity-velocity correlation function between the ith component of the initial velocity, $v_i(\mathbf{k},0)$, integrated over all possible starting points on the Fermi surface, and $v_j(\mathbf{k},t)$, the jth component of the velocity of a quasiparticle averaged over the duration of its orbit. The exponential term represents the probability of a quasiparticle scattering from its trajectory so that it no longer contributes to the conductivity.

Armed with the Chambers formula and Eq. (6), it is now possible to relate the way in which the program that simulates the interplane resistivity proceeds (a discussion of the possible errors that might creep in is left until the end): first, a quasiparticle is placed at point on the Fermi surface and its velocity components are found and recorded by differentiating Eq. (6), according to $\mathbf{v}=\hbar^{-1}\nabla_{\mathbf{k}}E(\mathbf{k})$.[30] Next, the Lorentz force ($\hbar d\mathbf{k}/dt=-e\mathbf{v}\times\mathbf{B}$, Ref. 30) for a given inclination of the magnetic field is allowed to act upon the quasiparticle for a short time so that it moves to a new position on the Fermi surface. Here its velocity components are again recorded and the process is repeated a large number of times so that a Fermi-surface orbit is mapped out.

The time-integral in the Chambers formula is obtained by multiplying each value of each velocity component by $\exp(-t/\tau)$ and adding the like components together. The scattering time τ is chosen to be 3 ps in order to reflect that measured from quantum oscillations and high-frequency conductivity measurements[9] and the whole orbit is recorded over a time $t=8\tau$, by which point more than 99.96% of the quasiparticles have been scattered. The time interval δt between points on an orbit was set to be quite small (never larger than 0.016τ) so that the sum of velocity components might approximate well to the integral in the Chambers formula. Each iteration of the simulation moves a quasiparticle on the Fermi surface a tiny amount in a direction dictated by the Lorentz force. The velocity of a quasiparticle at any point on the Fermi surface is perpendicular to the Fermi surface at that point, and the Lorentz force is always directed perpendicular to the quasiparticle velocity.[30] Thus the simulation moves the quasiparticle in a plane tangential to the Fermi surface. As the displacement of the quasiparticle at each iteration is small but not infinitesimal, the quasiparticle can deviate from the undulating Fermi surface by a tiny amount, the deviation accumulating over the course of many iterations. To combat this the Runge-Kutta method of solving ordinary differential equations is used to constrain the quasiparticles to the Fermi surface.[31]

The time-averaged velocity components are now multiplied by the relevant velocity component from the start of the process, i.e., $t=0$, and weighted by the density of states and the Fermi-surface area represented by the orbit. This routine is repeated for a large grid of starting points that span the entire first Brillouin zone, and the results are summed. In this way the integral over the Fermi surface in the Chambers formula is accomplished, and each component of the conductivity tensor is calculated. The results are combined to yield the interplane resistivity by inverting the conductivity tensor,

$$\rho_{zz}=\frac{\sigma_{xx}\sigma_{yy}-\sigma_{xy}\sigma_{yx}}{\sigma_{xx}\sigma_{yy}\sigma_{zz}-\sigma_{xx}\sigma_{yz}\sigma_{zy}+\sigma_{xz}\sigma_{yx}\sigma_{zy}-\sigma_{xy}\sigma_{yx}\sigma_{zz}+\sigma_{xy}\sigma_{yz}\sigma_{xz}-\sigma_{xz}\sigma_{yy}\sigma_{zx}}. \quad (8)$$

This method can be used to calculate the resistivity at any value of θ, ϕ, and B. The Fermi-surface resolution chosen, i.e., the number of orbits sampled, must be a compromise between the accuracy of the results and the speed of calculation. It is found that for θ angles away from 90° a grid of 100×100 starting points is sufficient to successfully simulate the resistivity. However, close to 90° the orbits are rapidly changing with θ, and the interplane resistivity is dominated

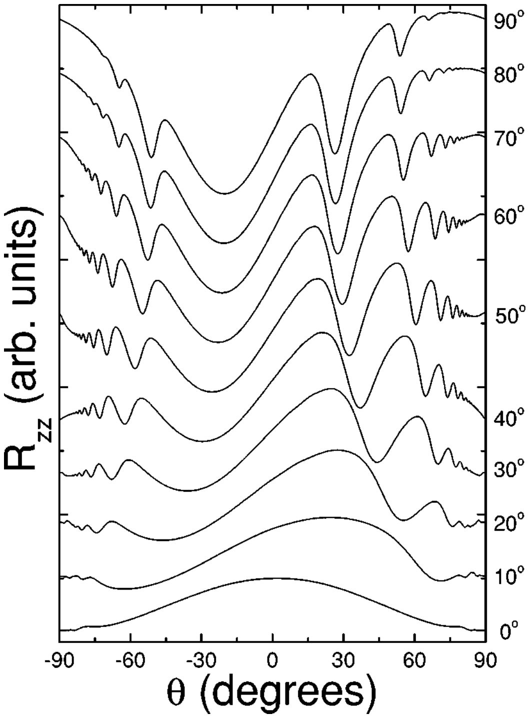

FIG. 7. The simulated interplane resistance resulting from solving the Chambers formula numerically for the Q1D Fermi-surface sheets of κ-(ET)$_2$Cu(NCS)$_2$, as described by Eq. (6). The θ dependences are shown for a fixed magnetic field of 42 T and a selection of values of the azimuthal angle ϕ. The Lebed magic angle effect dominates the magnetoresistance, except at low ϕ angles where the Danner-Kang-Chaikin oscillations are seen around $\theta = 90°$. The asymmetry of the curves reflects the monoclinic symmetry of the crystal structure.

by a few small, closely spaced orbits. In this case it is necessary to greatly increase the Fermi-surface resolution, which in turn greatly lengthens the duration of the simulation.

In performing these simulations the interest lies in their ability to reproduce the Lebed magic angle effect and the Yamaji oscillations, as it is these phenomena that need to be distinguished from one another. Less important are the Danner-Kang-Chaikin oscillations and the third angular effect. Although they too are reproduced by the Chambers formula, an analysis of these effects does not yield a great deal of useful information. That said, the in-plane peak effect, which is intimately related to both the Danner-Kang-Chaikin and third angular oscillations, is of great interest, but will be dealt with in a different manner in Sec. V D.

Simulations of the angle-dependence of the interplane resistivity at 42 T and several values of the azimuthal angle ϕ for the Q1D sections of Fermi surface are shown in Fig. 7. At $\phi = \pm 90°$, which corresponds to the magnetic field lying parallel to the Q1D sheets, the Lebed magic angle effect can be clearly seen as dips in the magnetoresistance. As the ϕ angle is changed the frequency of the dips also changes. At low ϕ angles the amplitude of the dips drops, and at $\phi = 0°$ they are no longer observed. The Danner-Chaikin oscillations are seen as smaller features near $\theta = 90°$ at low azimuthal angles.

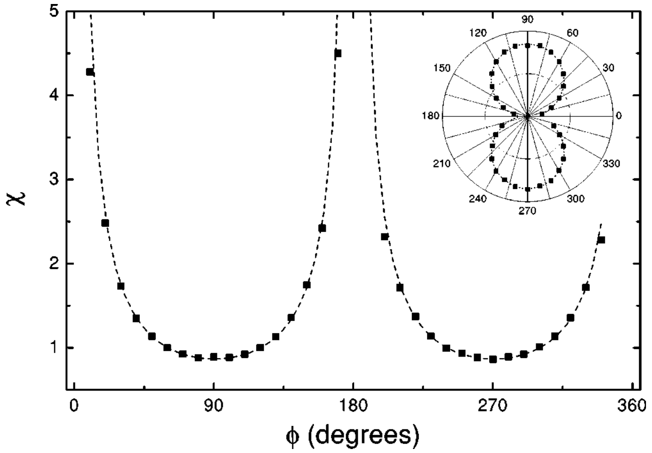

FIG. 8. The ϕ dependence of χ, deduced from the frequency of the simulated Lebed magic angle dips. The dotted line is a fit to Eq. (9). The insert shows the polar plot of $k_{\parallel}^{\max}$ vs ϕ that would result if the Q1D features were mistaken for Q2D Yamaji oscillations, with the dotted line representing a fit to Eq. (10).

The validity of these simulations can be checked by calculating the frequency in $(\tan\theta)^{-1}$, $1/\chi$, of the Lebed magic angle dips for each value of the azimuthal angle. In this way the ϕ dependence of χ can be fitted to the equation,

$$\chi(\phi) = \frac{\chi_0}{\cos(\phi - \phi_0)}, \tag{9}$$

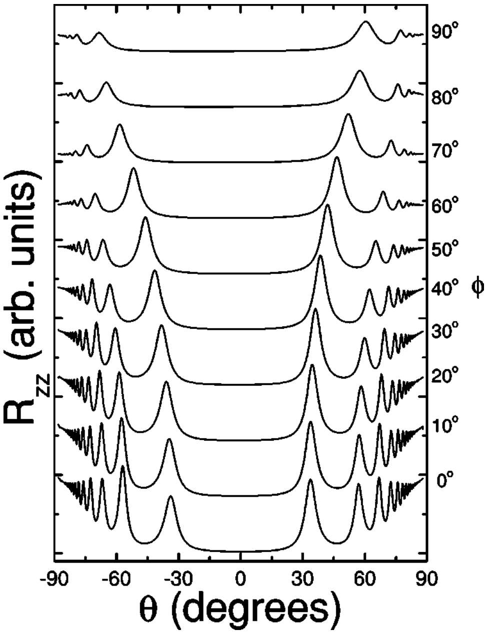

FIG. 9. The simulated interplane resistance resulting from solving the Chambers formula numerically for the Q2D Fermi-surface pockets of κ-(ET)$_2$Cu(NCS)$_2$, as described by Eq. (6). The θ dependences are shown for a fixed magnetic field of 42 T and a selection of values of the azimuthal angle ϕ. The Yamaji oscillations dominate the magnetoresistance, taking their maximum frequency when the in-plane field is applied along $\phi = 0°$, which is parallel to the major axis of the Q2D pocket.

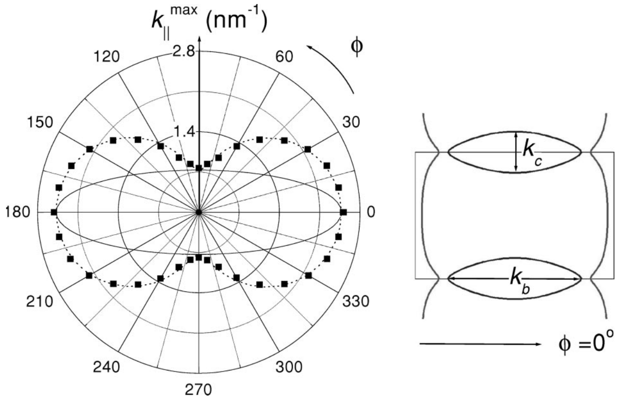

FIG. 10. Left: The data points are the $k_\parallel^{\max}$ values as obtained from the frequency of the Q2D Yamaji oscillations in the simulated resistance, the dotted line is a fit to Eq. (10), and the solid line is the resulting Fermi-surface pocket. Right: A reminder of the in-plane Fermi surface of κ-(ET)$_2$Cu(NCS)$_2$.

where ϕ_0 corresponds to the magnetic field lying parallel to the Q1D sheets.[32] The results of such an analysis are shown in Fig. 8. From the fit the value of χ_0, which is equal to the c lattice parameter divided by the interlayer distance, $d_\perp$, is found to be 0.8658 ± 0.0005. This can be compared with the value of $c/d_\perp = 0.861 \pm 0.001$ obtained from x-ray scattering measurements.[7]

The inset to Fig. 8 shows the results of analyzing the Lebed magic angles if they were mistakenly taken for Yamaji oscillations. The dotted line is a fit to the equation,

$$k_\parallel^{\max}(\phi) = [k_a^2 \cos^2(\phi - \xi) + k_b^2 \sin^2(\phi - \xi)]^{1/2}, \qquad (10)$$

which is valid for a Fermi surface with an elliptical cross section and where $k_\parallel^{\max}$ is the maximum in-plane Fermi wave vector projected on the plane of rotation of the field and is found from the frequency of the Yamaji oscillations. k_a and k_b are the major and minor semiaxes of the Q2D Fermi-surface pocket, respectively.[33] This fit suggests the existence of an elliptical Q2D pocket with major and minor axes of 2.37 nm^{-1} and 0.29 nm^{-1}, respectively. If these were experimental results then it is easy to see that in the absence of any other evidence such a Fermi-surface pocket might seem quite reasonable. However, the mistake becomes apparent when the fundamental frequency of the quantum oscillations that would be expected from a closed pocket of this size, 227 T, is compared with the experimentally determined value of 599 T.

Figure 9 shows the simulated interplane magnetoresistance that arises from the Q2D closed Fermi-surface pockets at 42 T and various ϕ angles. It is seen that the traces are dominated by the peaks of the Yamaji oscillations. $k_\parallel^{\max}$ can be extracted from the frequency of the oscillations at each ϕ angle, and the result of fitting this to Eq. (10) is shown in Fig. 10. The resulting Q2D pocket has a major axis k_b of 2.476 ± 0.001 nm^{-1}, and a minor axis k_c of 0.733 ± 0.002 nm^{-1}. This would give rise to quantum oscillations with a fundamental frequency of 598 T, which is in agreement with the value measured from the SdH effect.

It is now possible to mark the differences expected between the shape of the Q2D pocket that results from the correct analysis of the Yamaji angles, and that from the mistaken identification of the Lebed magic angles. The obvious difference is that the pockets are perpendicular to each other, with the long axis of the true Q2D pocket lying along the $\phi = 0°$ direction. If the samples used in the experiments had been oriented by optical measurements then this would be sufficient to distinguish the AMRO. However, this is not the case. The major axes of the two alleged pockets are similar to each other, and an experimental error is likely to encompass them both. Thus it is to the minor axis that one must look to separate the two AMRO effects.

All in all, the simulations agree very well with the experimental results of both x-ray scattering and the SdH effect. Nevertheless, it is worthwhile to look more closely at the various errors that might be introduced into the simulation process along the way. The first most general problem to be addressed is that the simulations are semiclassical, and take no account of the quantum oscillations and, more importantly, the magnetic breakdown. As the perpendicular field is increased to high magnitudes, the experimentally measured AMRO will become affected by magnetic breakdown, as more and more Q1D carriers tunnel through the energy gap and become Q2D carriers. Eventually, the system will resemble one large Q2D Fermi surface pocket whose cross section in the highly conducting planes is the β orbit. However, AMRO tend to be the most concentrated near to $\theta = 90°$. In fact, the actual experiments were performed at 42 T, and it will be seen that almost all the important AMRO features occur at θ angles of around 70° or higher. The perpendicular magnetic field at $B = 42$ T, $\theta = 70°$ is such that for the $d8$ sample less than 1 quasiparticle in 14 has sufficient energy to bridge the gap between the Fermi surfaces. For $h8$ this value is less than 1 in 50, and the probability of breakdown for both types of sample decreases towards zero as θ approaches 90° (whether or not the probability actually reaches zero at $\theta = 90°$ depends on the relative sizes of t_a and E_g). Thus for the current situation the magnetic breakdown is only a minor consideration.

The most likely entry point for errors to make their way into the calculations is via the values chosen to represent the various physical parameters. It has already been mentioned that the values chosen for t_b, t_c, and E_{F} used in conjunction with the effective dimer model reproduce the measured Fermi surface very well, so attention is turned to the other parameters, namely, E_g and t_a. The value of 7.8 meV chosen for E_g is derived from a measured value of the magnetic breakdown, which has a large error associated with it.[20] However, a quick glance at how such an error propagates reveals it to be relatively unimportant: E_g represents the gap in k space between the Q1D and Q2D sections of Fermi surface, and an order of magnitude estimate of this gap in terms of wave vector Δk is given by $\Delta k / k_{\mathrm{F}} \sim E_g / E_{\mathrm{F}}$.[19] Using estimates for k_{F} and E_{F},[2] it is found that $\Delta k \sim 0.4$ nm^{-1}. As the area of the Q2D pocket is well defined, any error on the size of the gap would lead to errors in k_b and k_c, the axes that define the pocket. A generous error on k_b is ± 0.2 nm^{-1}, or half of Δk, which represents what would

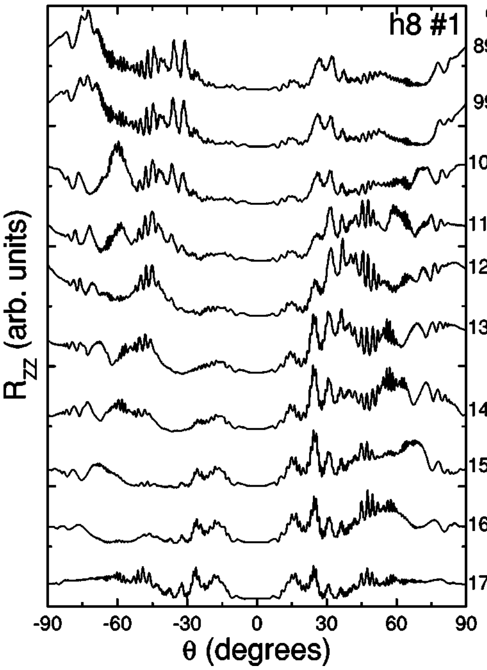

FIG. 11. The angle-dependent interlayer magnetoresistance of $h8$ κ-$(ET)_2Cu(NCS)_2$ at various values of the azimuthal angle ϕ. $T \approx 500$ mK and $B = 42$ T.

happen if the energy gap were allowed to be zero. Fixing the area, this leads to an error of around ± 0.1 nm^{-1} on k_c. Even with such an uncertainty on the magnitude of the minor axis, it would still be possible to distinguish between the results arising from the Yamaji oscillations and those from the Lebed magic angles.

The value used to represent t_a, the transfer integral along the crystallographic a direction, is based on a preliminary analysis of the in-plane peak effect.[9] As it is quite small, 0.04 meV, it is likely to have associated with it a significant relative error. However, the positions of the AMRO features arising from the Yamaji and Lebed effects are unaffected by the magnitude of the t_a parameter. In the current situation the amplitudes of the oscillations are of little concern, thus, for the moment, neither is the precise value t_a.

2. Experiments

Figure 11 shows a selection of the measured angle dependences of $h8$ κ-$(ET)_2Cu(NCS)_2$, at various values of the azimuthal angle, in a field of 42 T and at temperatures around 500 mK. In order to analyze such angle dependences, the position of each AMRO peak and dip is recorded. The frequency in $(\tan\theta)^{-1}$ of the peaks and dips at each ϕ angle is then found for each sample, and the results are compared to those obtained from the simulated resistance. The AMRO arising from the Q1D and Q2D Fermi surfaces are thus identified and the measured ϕ angle can be calibrated so that $\phi = 0°$ is perpendicular to Q1D sheets. The frequencies of the dips arising from the Q1D Lebed magic angle effect for each sample are combined and fitted to Eq. (9). The result is shown in the top part of Fig. 12. The fit is good and it is found that $\chi_0(h8) = c/d_\perp = 0.89 \pm 0.10$, which is in reasonable agreement with value of 0.861 ± 0.001 found from x-ray scattering.[7]

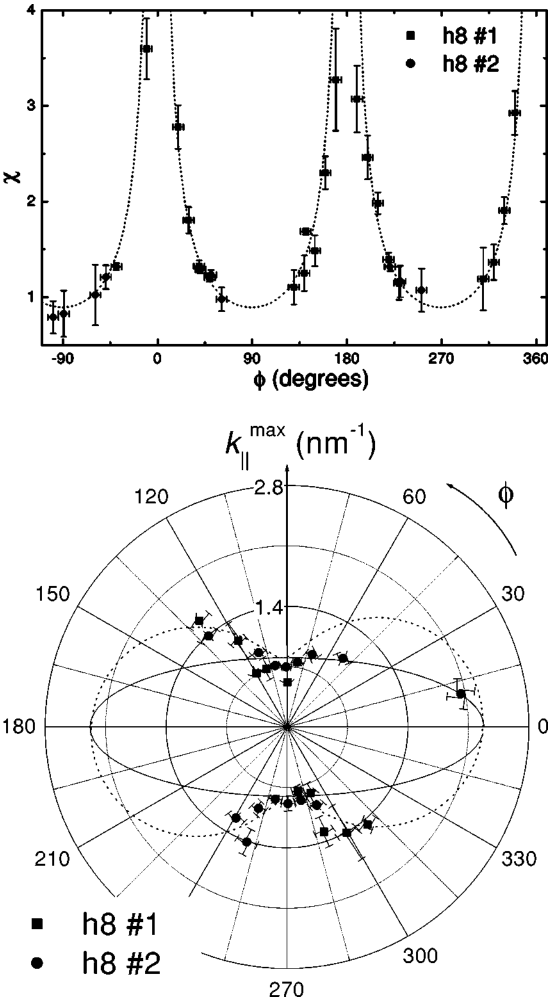

FIG. 12. Top: The value of χ, obtained from the frequency of the resistance dips caused by the Lebed magic angle effect, at various values of the calibrated azimuthal angle ϕ. The dotted line is a fit to Eq. (9). Bottom: The values of $k_\parallel^{max}(\phi)$, obtained from a Yamaji analysis of the peaks in resistance, at various values of the calibrated azimuthal angle ϕ. The dotted line is a fit to Eq. (10) constrained so that the resulting Q2D pocket (solid line) has an area corresponding to the measured fundamental frequency. In both figures the squares are the data from $h8$ sample No. 1, the circles are the data from $h8$ sample No. 2.

The results of calculating $k_\parallel^{max}(\phi)$ for the resistance peaks arising from the Q2D Yamaji oscillations for each sample are also combined, and these data, together with the curve obtained by fitting to Eq. (10), are shown in the bottom part of Fig. 12.

It is seen that almost all the $k_\parallel^{max}(\phi)$ data are concentrated around the region where the magnetic field is roughly perpendicular to the flattish portion of the Q2D pocket—at the other ϕ angles, the resistance is dominated by the Lebed effect. This means that the major axis k_b is ill-defined and it is necessary when performing the fit to fix the area of the pocket so that it reproduces the measured fundamental fre-

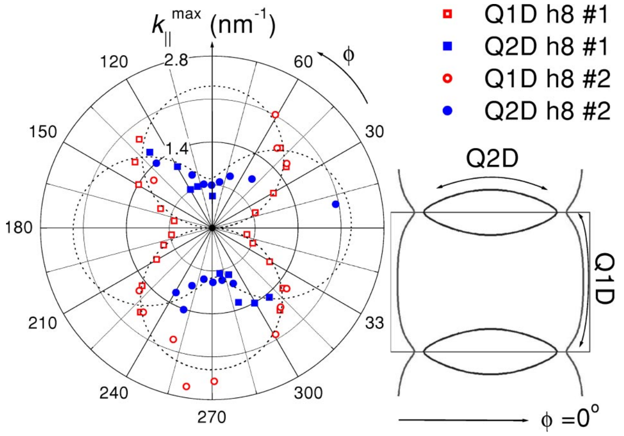

FIG. 13. The result of analyzing all the AMRO as if they were Yamaji oscillations. The squares are the data from $h8$ sample No. 1, the circles are the data from $h8$ sample No. 2, the hollow symbols are the data from Lebed magic angle dips, the solid symbols are the data from Yamaji peaks, and the dotted lines are the fitted curves from Fig. 12. This shows that the Q1D effects dominate when the field is nearly perpendicular to the sheets, and the Q2D effects dominate when the field is nearly perpendicular to the flatter edge of the Fermi-surface pockets.

quency of the SdH oscillations. It can be seen from the figure that this fit is reasonable; and the results obtained are $k_c(h8) = 0.80 \pm 0.05$ nm^{-1} and $k_b(h8) = 2.28 \pm 0.15$ nm^{-1}.

It is illustrative to calculate $k_\parallel^{\max}(\phi)$ for all the $h8$ data (Lebed angles and Yamaji oscillations) and display the results on the same polar plot. In this way it is easy to see which Fermi-surface section dominates the resistance at a given azimuthal angle. This plot is shown in Fig. 13. The hollow symbols are the Lebed magic angle dips and the solid symbols are the Yamaji peaks. The dotted lines are the fitted curves from the previous two figures. It is clear that the Q1D Fermi-surface sheets dominate the angle-dependent magnetoresistance when the field is roughly perpendicular to the sheets, and the Q2D pockets dominate when the field is roughly perpendicular to their flatter edges.

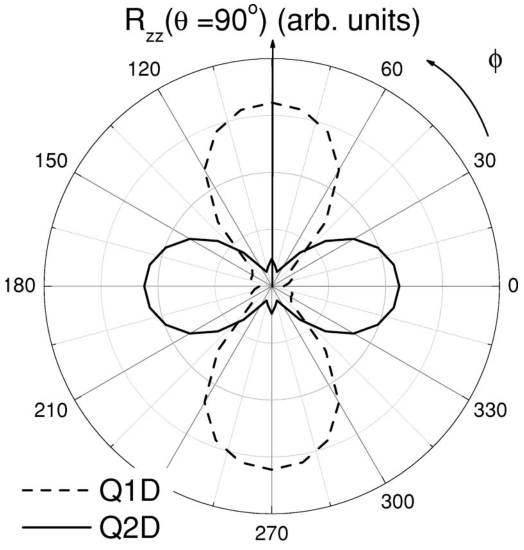

FIG. 14. ϕ dependence of the simulated interlayer resistance at $\theta = 90°$ for both the Q1D and Q2D sections of Fermi surface at a fixed field of 42 T. This is the same geometry as the third angular effect.

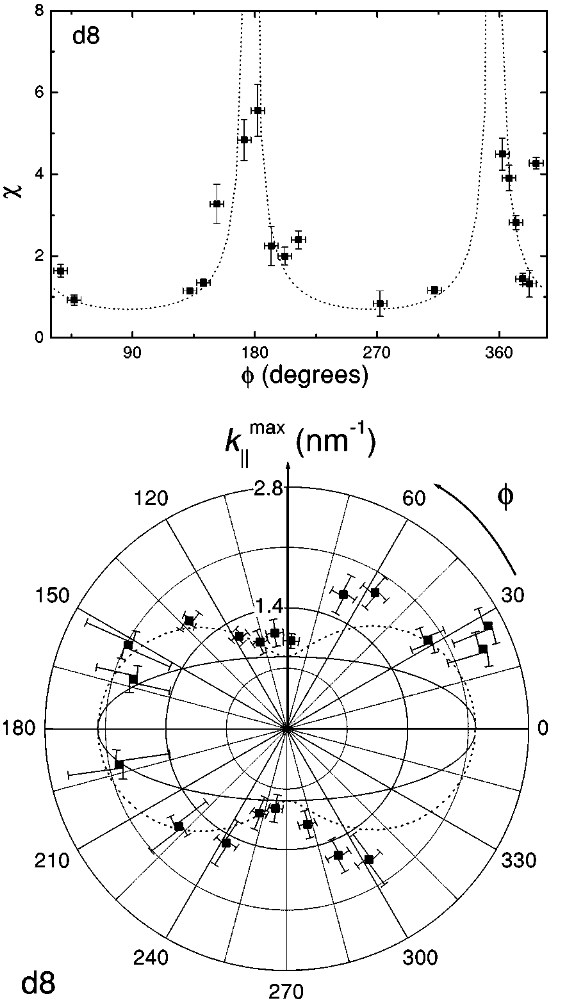

FIG. 15. Results for the $d8$ sample. Top: The value of χ, obtained from the frequency of the resistance dips caused by the Lebed magic angle effect, at various values of the calibrated azimuthal angle ϕ. The dotted line is a fit to Eq. (9). Bottom: The values of $k_\parallel^{\max}(\phi)$ obtained from an Yamaji analysis of the peaks in resistance at various values of the calibrated azimuthal angle ϕ. The dotted line is a fit to Eq. (10) constrained so that the resulting Q2D pocket (solid line) has an area corresponding to the measured fundamental frequency.

In order to shed light on this behavior, Fig. 14 shows the result of simulating the interlayer resistance at fixed field of 42 T and a θ angle of 90° over the whole range of azimuthal angle, for both the Q1D and Q2D Fermi-surface sections. This is just the simulated third angle effect plotted in polar coordinates, and is chosen to be representative of the magnitude of the resistance at 42 T in the angular region (70°–90°) over which AMRO are observed. By qualitatively comparing Figs. 13 and 14, it is seen that the range of azimuthal angles over which the Q1D Fermi surface dominates the measured magnetoresistance is similar to that over which the simulated $R_{zz}(\theta = 90°)$ due to the Q1D sheets is lower than

TABLE I. Comparison of results derived from the AMRO of $h8$ and $d8$ κ-(ET)$_2$Cu(NCS)$_2$, and from the semiclassical transport simulations.

	χ_0	k_b (nm^{-1})	k_c (nm^{-1})
$h8$	0.89±0.10	2.28±0.15	0.80±0.05
$d8$	0.70±0.15	2.19±0.35	0.83±0.13
Simulations	0.8658±0.0005	2.476±0.001	0.733±0.002

that due to the Q2D pockets. The inverse is true for the range of angles where the measured magnetoresistance is dominated by Q2D AMRO effects. This observation indicates that the resistances from the two sections of Fermi surface could combine in a similar way to resistors in parallel, i.e., the overall resistance of the system at a given ϕ angle is dominated by the section of Fermi surface that takes the lowest resistance at that angle. However, the situation away from $\theta = 90°$ is not quite as simple as the parallel resistors scenario, as it is found that adding the simulated angle-dependent resistances for each Fermi-surface section using $R_{\mathrm{total}}^{-1} = R_{\mathrm{Q1D}}^{-1} + R_{\mathrm{Q2D}}^{-1}$ does not successfully reproduce the experimental results. This result is not unexpected as the magnetic breakdown, which will become more pronounced away from $\theta = 90°$ and acts to transfer quasiparticles from one surface to the other, has not been taken into account. Also the conductivities of each Fermi-surface section would need to be summed before the conductivity matrix is inverted and the resistivity obtained. However, doing this would mean that individual features in the magnetoresistance could not be associated with a particular Fermi-surface section, which is one of the driving forces behind performing these simulations.

Similar AMRO effects were measured in the $d8$ sample. The top part of Fig. 15 shows the azimuthal angle dependence of the frequency of the Lebed magic angle dips. The fit to Eq. (9) is reasonable but not nearly as good as that for the $h8$ sample. The value of $\chi_0(d8) = c/d_\perp$ is found to be 0.70 ±0.15. This can be compared to the value of 0.862±0.001 found from x-ray scattering measurements of the deuterated salt.[34] It is not entirely clear why the results are not as successful for the $d8$ sample as for the $h8$; however, it is seen that there are nearly half the number of data points in the $d8$ fit compared to that of the $h8$, and further, the density of points in the regions around $\phi = 90°$, where the χ_0 parameter is best defined, is much lower in the case of the $d8$ fit.

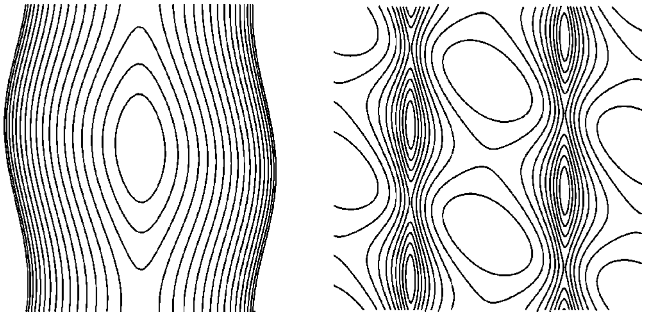

FIG. 16. Examples of the orbits possible on the Q2D (left) and Q1D (right) sections of the Fermi surface defined by Eq. (6) when the magnetic field is applied parallel to the highly conducting planes. All the orbits tend to average the interlayer velocity to zero, and hence produce an increase in the interlayer resistance. For the purposes of the illustration, the interlayer transfer integral has been exaggerated compared to its experimentally determined value.

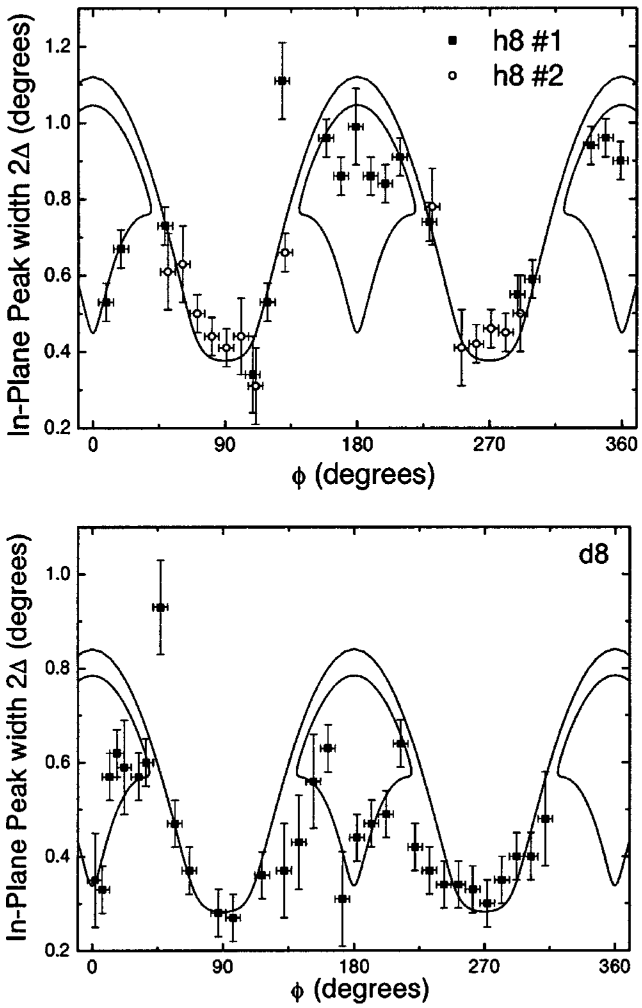

FIG. 17. Azimuthal angle dependence of the angular width 2Δ of the in-plane peak for $h8$ (top) and $d8$ (bottom) κ-(ET)$_2$Cu(NCS)$_2$ at $B = 42$ T, $T \approx 500$ mK. The points are the experimentally measured widths and the solid lines are the simulated width with $t_a(h8) = 0.065 \pm 0.007$ meV and $t_a(d8) = 0.045 \pm 0.005$ meV. The continuous curve represents the contribution from the Q2D Fermi-surface pockets, whereas the closed curves are those from the Q1D sheets.

The bottom part of Fig. 15 shows the azimuthal angle dependence of $k_\parallel^{\max}$ as calculated from the frequency of the Yamaji oscillations. In order to fit the data to Eq. (10), the area is again constrained to produce quantum oscillations of the correct frequency. The axes of the pocket are thus found to be $k_c(d8) = 0.83 \pm 0.13$ nm^{-1} and $k_b(d8) = 2.19 \pm 0.35$ nm^{-1}.

A comparison of the results of analyzing the AMRO measured in the $h8$ and $d8$ samples, and those simulated using the Chambers Formula, is shown in Table I. It is seen that the results for $h8$ and $d8$ agree with each other within the error ranges. It is also seen that there is a reasonable correlation between the experimentally determined values and those from the simulations. This implies that the parameters used in the simulation program are good approximations to the real values, and that it is possible to explain the AMRO in terms of purely semiclassical effects.

D. Characterizing the interlayer transport

For a system with a three-dimensional Fermi surface, a series of quasiparticle orbits are possible in the presence of an exactly in-plane magnetic field, many of which are very good at averaging the interlayer velocity towards zero (see Fig. 16). This is the origin of the in-plane peak effect in ρ_{zz}, and suggests a coherent nature to the interlayer transport.[35,36]

For highly anisotropic materials, the angular width 2Δ of the in-plane peak, when measured in radians, can be approximated by $2v_{\perp}^{\max}/v_{\parallel}$, where $v_{\perp}^{\max}$ is the maximum of the out-of-plane component of the quasiparticle velocity and $v_{\parallel}$ is the in-plane component parallel to the plane of rotation of the magnetic field.[9] The ϕ dependence of $v_{\parallel}$ can be calculated for κ-(ET)$_2$Cu(NCS)$_2$ using the dispersion relation in Eq. (6) and the in-plane Fermi-surface parameters discussed in Sec. III. $v_{\perp}$ is given by $\hbar^{-1}\partial E/\partial k_z$, and so $v_{\perp}^{\max}$ is a constant equal to $2t_a a\cos(\beta-\pi/2)/\hbar$. In this way 2Δ is calculated, with the value of t_a left as the only adjustable parameter. This value is determined by comparing the results of the calculation with the experimentally derived values for the width of the in-plane peak. This is the same method used in Ref. 9; however, in the present case the monoclinic structure of κ-(ET)$_2$Cu(NCS)$_2$ is taken into account, and hence slightly different results are achieved.

The result for the $h8$ sample is shown in the top part of Fig. 17. Here the points are the experimental data for two $h8$ samples, and the solid lines are the results of the calculations obtained by setting $t_a(h8)=0.065\pm0.007$meV. The continuous curve arises from closed orbits on the Q2D FS pocket, which are possible when the magnetic field is directed along any ϕ angle. The closed loops correspond to orbits about the Q1D FS sheets, which are only possible when the field is directed along a limited range of ϕ. Away from this ϕ range the data follows the continuous curve fairly well and agrees with the ϕ calibration found in the preceding section. Around $\phi=0°$, 180°, and 360° the width of the peak can be governed by any of the three sets of closed orbits possible; those on the broadly curved, convex region of Q1D sheets; those on the pointed, concave region located at the Brillouin zone boundary; or those on the Q2D pocket. The way in which these orbits will combine to produce the in-plane peak is not entirely clear, but it might be expected that the conductivities of each orbit sum to produce the total conductivity, as is the case in the Chambers formula. To the first approximation, the off-diagonal components of the conductivity may be ignored, thus the interlayer resistivity is found by inverting the interlayer conductivity and so,

$$\frac{1}{\rho_{zz}}\approx\sigma_{zz}=\sigma_{zz_1}+\sigma_{zz_2}+\sigma_{zz_3}+\cdots$$
$$\approx\frac{1}{\rho_{zz_1}}+\frac{1}{\rho_{zz_2}}+\frac{1}{\rho_{zz_3}}+\cdots, \qquad (11)$$

i.e., the resistivity contributions from each orbit combine like resistors in parallel, and it is the path with the smallest resistivity that dominates the total resistance. Thus, in terms of the in-plane peak effect it may be expected that the orbits that are the least efficient at averaging the interlayer velocity towards zero will dominate the resistance.

The results for the $d8$ sample are shown in the bottom part of Fig. 17. The best agreement between calculations and experiment was found by setting $t_a(d8)=0.045\pm0.005$ meV.

VI. CONCLUSIONS

In summary, several physical properties have been measured for both hydrogenated and deuterated κ-(ET)$_2$Cu(NCS)$_2$. No disparity has been found in the size and shape of the Fermi surfaces of the two isotopes, their effective masses, their scattering rates, or their energy-level structures. The only discernable difference found was in the interlayer transfer integral, which appeared lower for the deuterated salt.

The size of the interlayer warping is determined by the transfer integral in this direction. An increased warping means that the Fermi surface will be less able to nest. Thus, if indeed the superconductivity in this material is aided by nestability[3–5] then the higher transfer integral in the $h8$ salt would help to explain its lower superconducting transition temperature.

Further, it has been shown that the measured angle-dependent magnetoresistance oscillations can be reproduced via purely semiclassical, Boltzmann transport considerations. The observed peak in the resistance in the presence of a nearly in-plane magnetic field suggests that at low temperatures and ambient pressure the Fermi surface of κ-(ET)$_2$Cu(NCS)$_2$ is a three-dimensional object that extends throughout the reciprocal space. Thus it is not necessary to invoke non-Fermi liquid effects in order to describe the angle-dependent interlayer transport in this material.

ACKNOWLEDGMENTS

This work was supported by EPSRC (UK). NHMFL was supported by the U.S. Department of Energy (DOE), the National Science Foundation, and the State of Florida. Work at Argonne was sponsored by the DOE, Office of Basic Energy Sciences, Division of Materials Science under Contract No. W-31-109-ENG-38.

*Electronic address: pgoddard@lanl.gov

[1] T. Sasaki, H. Sato, and N. Toyota, Solid State Commun. **76**, 507 (1990).

[2] T. Sasaki, H. Sato, and N. Toyota, Physica C **185-189**, 2687 (1991).

[3] J. Schmalian, Phys. Rev. Lett. **81**, 4232 (1998).

[4] H. Kondo and T. Moriya, J. Phys. Soc. Jpn. **67**, 3695 (1998).

[5] K. Kuroki and H. Aoki, Phys. Rev. B **60**, 3060 (1999).

[6] J.A. Schlueter, A.M. Kini, B.H. Ward, U. Geiser, H.H. Wang, J. Mohtasham, R.W. Winter, and G.L. Gard, Physica C **351**, 261 (2001).

[7] H. Urayama, H. Yamochi, G. Saito, K. Nozawa, T. Sugano, M. Kinoshita, S. Sato, K. Oshima, A. Kawamoto, and J. Tanaka, Chem. Lett. **1988**, 55 (1988).

[8] J. Caulfield, W. Lubczynski, F.L. Pratt, J. Singleton, D.Y.K. Ko, W. Hayes, M. Kurmoo, and P. Day, J. Phys.: Condens. Matter **6**, 2911 (1994).

[9] J. Singleton, P.A. Goddard, A. Ardavan, N. Harrison, S.J. Blundell, J.A. Schlueter, and A.M. Kini, Phys. Rev. Lett. **88**, 037001 (2002).

[10] R.J. Nicholas, R.J. Haug, K. v Klitzing, and G. Weimann, Phys. Rev. B **37**, 1294 (1988).

[11] G.M. Danner, W. Kang, and P.M. Chaikin, Phys. Rev. Lett. **72**, 3714 (1994).

[12] T. Osada, S. Kagoshima, and N. Miura, Phys. Rev. Lett. **77**, 5261 (1996).

[13] S.J. Blundell and J. Singleton, Phys. Rev. B **53**, 5609 (1996).

[14] V.G. Peschansky, J.A.R. Lopez, and T.G. Yao, J. Phys. I **1**, 1469 (1991).

[15] M.V. Kartsovnik, V.N. Laukhin, S.I. Pesotskii, I.F. Schegolev, and V.M. Yakovenko, J. Phys. I **2**, 89 (1992).

[16] A.G. Lebed, Synth. Met. **70**, 993 (1995).

[17] P.M. Chaikin, Phys. Rev. Lett. **69**, 2831 (1992).

[18] J. Singleton, J.A. Symington, M.-S. Nam, A. Ardavan, M. Kurmoo, and P. Day, J. Phys.: Condens. Matter **12**, L641 (2000).

[19] D. Shoenberg, *Magnetic Oscillations in Metals* (Cambridge University Press, Cambridge, 1984).

[20] N. Harrison, J. Caulfield, J. Singleton, P.H.P. Reinders, F. Herlach, W. Hayes, M. Kurmoo, and P. Day, J. Phys.: Condens. Matter **8**, 5415 (1996).

[21] N. Harrison, E.J. Rzepniewski, J. Singleton, S.J. Blundell, and F. Herlach, J. Phys.: Condens. Matter **11**, 7227 (1999).

[22] P.A. Goddard, S.W. Tozer, J. Singleton, A. Ardavan, A. Abate, and M. Kurmoo, J. Phys.: Condens. Matter **14**, 7345 (2002).

[23] T. Biggs, A.-K. Klehe, J. Singleton, D. Bakker, J. Symington, P.A. Goddard, A. Ardavan, W. Hayes, J.A. Schlueter, T. Sasaki, and M. Kurmoo, J. Phys.: Condens. Matter **14**, 495 (2002).

[24] G.N. Kamm, J. Appl. Phys. **49**, 5951 (1978).

[25] N. Harrison, R. Bogaerts, P.H.P. Reinders, J. Singleton, S.J. Blundell, and F. Herlach, Phys. Rev. B **54**, 9977 (1996).

[26] J. Singleton, Rep. Prog. Phys. **63**, 1111 (2000).

[27] J. Wosnitza, G. Goll, D.B.S. Wanka, D. Schweitzer, and W. Strunz, J. Phys. I **6**, 1597 (1996).

[28] Equation (6) differs from the dispersion relation quoted in Ref. 9 because in the present paper the monoclinic structure of κ-$(\mathrm{ET})_2\mathrm{Cu(NCS)}_2$ ($\beta = 110.30 \pm 0.03°$, Ref. 7) is taken into account.

[29] R.G. Chambers, Proc. Phys. Soc. London **A65**, 458 (1952).

[30] N.W. Ashcroft and A.D. Mermin, *Solid State Physics* (Saunders College Publishing, Orlando, 1976).

[31] J.D. Lambert, *Numerical Methods for Ordinary Differential Systems: The Initial Value Problem* (Wiley, New York, 1997), Chap. 5.

[32] J. Caulfield, S.J. Blundell, M.S.L. du Croo de Jongh, P.T.J. Hendriks, J. Singleton, M. Doporto, F.L. Pratt, A. House, J.A.A.J. Perenboom, W. Hayes, M. Kurmoo, and P. Day, Phys. Rev. B **51**, 8325 (1995).

[33] A.A. House, N. Harrison, S.J. Blundell, I. Deckers, J. Singleton, F. Herlach, W. Hayes, J.A.A.J. Perenboom, M. Kurmoo, and P. Day, Phys. Rev. B **53**, 9127 (1996).

[34] G. Saito, H. Yamochi, T. Nakamura, T. Komatsu, T. Ishiguro, Y. Nogami, Y. Ito, H. Mori, K. Oshima, M. Nakashima, S. Uchida, H. Takagi, S. Kagoshima, and T. Osada, Synth. Met. **41-43**, 1993 (1991).

[35] R.H. McKenzie and P. Moses, Phys. Rev. Lett. **81**, 4492 (1998).

[36] N. Hanasaki, S. Kagoshima, T. Hasegawa, T. Osada, and N. Miura, Phys. Rev. B **57**, 1336 (1998).